Nanoscale Advances

This article can be cited before page numbers have been issued, to do this please use: M. M. Hammo, S. Froeschke, G. Haider, D. Wolf, A. A. Popov, B. Büchner, M. Mertig and S. Hampel, *Nanoscale Adv.*, 2025, DOI: 10.1039/D4NA00935E.

View Article Online
DOI: 10.1039/D4NA00935E

Novel Synthesis Approach of Highly Crystalline $CrCl_3/MoS_2$ van der Waals Heterostructures Unaffected by Strain

Mahmoud M. Hammo *[ab], Samuel Froeschke [a], Golam Haider [a], Daniel Wolf [a], Alexey Popov [a], Bernd Büchner [a,c], Michael Mertig [b,d], Silke Hampel [a]

[a] Leibniz Institute for Solid State and Materials Research Dresden, Helmholtzstraße 20, 01069 Dresden, Germany

[b] Institute of Physical Chemistry, Technische Universität Dresden, 01062 Dresden, Germany

[c] Institute of Solid State and Materials Physics, Technische Universität Dresden, Dresden, Germany

[d] Kurt-Schwabe-Institut für Mess- und Sensortechnik Meinsberg e.V., Kurt-Schwabe-Straße 4, Waldheim 04736, Germany

Corresponding Author *E-mail: m.hammo@ifw-dresden.de

Tel: +4917687315637

ABSTRACT

View Article Online
DOI: 10.1039/D4NA00935E

Controlling the layer-by-layer chemistry and structure of nanomaterials remains a crucial focus in nanoscience and nanoengineering. Specifically, the integration of atomically thin semiconductors with antiferromagnetic two-dimensional materials holds great promise for advancing research. In this work, we successfully demonstrate a new synthesis approach of high-crystallinity $CrCl_3/MoS_2$ van der Waals heterostructures via a thermodynamically optimized chemical vapor transport (CVT) process on *c*-sapphire (0001) substrates. The 2H-MoS_2 layers can be grown as monolayer or with varying twist angles whereas the deposition of $CrCl_3$ layers in a second step forms the well-defined heterostructure. Of particular significance are the sharp and clean edges and faces of the crystals, indicating high-quality interfaces of the heterostructures. Raman spectroscopy, AFM and HRTEM confirm the monocrystalline character and precise structure of these layered nanomaterials, which their intrinsic properties are preserved, unaffected by strain. This can pave the way for next-generation applications, particularly in valleytronics, opto-spintronics, and quantum information processing.

View Article Online
DOI: 10.1039/D4NA00935E

INTRODUCTION

The exceptional properties van der Waals (vdW) heterostructures, which comprise atomically thin layered materials such as graphene, transition metal trihalides (TMTHs), transition metal dichalcogenides (TMDCs) and various topologically layered materials, have paved the way for a wide range of innovative research opportunities, encompassing both fundamental and applied research [1-6]. These heterostructures are predominantly created by stacking two-dimensional (2D) materials layer-by-layer. The weak vdW forces enable the assembly of dissimilar materials without the constraints of lattice matching [7]. A number of studies have demonstrated that the incorporation of a monolayer (ML) of TMDCs into 2D materials, including WSe_2/$CrBr_3$, can lead to a notable alteration in their optoelectronic properties [8-12]. However, the synthesis of strain-free heterostructures remains an intriguing area of study. By employing a synthesis method that mitigates strain, we ensure that the intrinsic properties of layers are preserved, resulting in high-quality interfaces with minimal defects. The strain-free synthesis method is driven by its significance for practical applications, particularly in valleytronics, opto-spintronics, and quantum information processing. In valleytronic devices, the ability to manipulate electron populations in distinct energy valleys of 2D semiconductors like MoS_2 is crucial. Strain-induced distortions can shift these valleys, reducing device efficiency and stability [13]. The strain-free growth ensures that the valleys remain well-defined, enabling robust valley-dependent charge transport and optical transitions. In addition to the well-studied heterostructure WSe_2/$CrBr_3$, the construction and investigation of the similar heterostructure $CrCl_3$/MoS_2 is also very promising, for example to explore phenomena such as the spin proximity effect. The combination of a 2D semiconductor (MoS_2) and a layered A-type antiferromagnetic insulator ($CrCl_3$) [14-16] forms a promising heterostructure for opto-spintronics. The direct bandgap of MoS_2 supports efficient light emission and absorption, while $CrCl_3$ provides magnetic ordering. This enables optical control of spin and valley degrees of freedom, paving the way for spin-based photonic devices and memory elements [17]. Therefore, combination these types of materials continues to generate significant interest among physicists, chemists and material scientists [18-21], and represents an effective approach to developing highly functional materials for spintronic and opto-spintronic applications [19,22]. High-quality, strain-free interfaces are essential for fabricating devices that leverage quantum

View Article Online
DOI: 10.1039/D4NA00935E

coherence. In heterostructures where spin-orbit coupling or exciton recombination is involved, strain can introduce unwanted decoherence or scatter carriers [23].

Two principal approaches are typically applied for the fabrication of vdW heterostructures. The first one is a top-down approach, which encompasses techniques such as exfoliation from the bulk/single crystal, and subsequent, assembly through utilization of standard dry transfer techniques [18-20, 24-27]. This approach does not allow for precise control over the number of layers, which limits its overall significance. In addition to the time consuming, this approach presents other disadvantages, including damage of the edge structure and contamination of the cleaved interfaces. Furthermore, the presence of process-related impurities at the interface, including polymers residues [28], water and air bubbles [29], impedes the efficient formation of heterostructures. This significantly affects the overall quality of the heterostructure [30].

The second approach is a bottom-up method, in which such heterostructures are commonly grown using techniques such as chemical vapor deposition (CVD) [31, 32], physical vapor deposition (PVD) [33], or various epitaxial processes. These methods are particularly well-suited to the production of heterostructures with high-quality, clean, and atomically sharp interfaces. While the synthesis via CVD or PVD requires rather complex equipment, the synthesis via CVD is a highly cost-effective and straightforward process. Instead of these methods, and for the first time, sequential chemical vapor transport (CVT) was employed to prepare the 2D vdW heterostructures. Sequential CVT comprises two consecutive steps. Each step is designed to achieve a specific part of the total vdW heterostructure growth. The optimal parameters (e.g. precursor deposition, temperature gradient ΔT, residence time and transport time) have to be identified for each individual step.

This study describes a scalable two-step vapor phase growth process for the fabrication of highly crystalline, vertically stacked $CrCl_3/MoS_2$ heterostructures on *c*-sapphire (Al_2O_3) substrates oriented along (0001) direction. Different growth temperatures and times have been evaluated, and the best conditions have been identified. Theoretical studies of gas phase composition and equilibria support the experimental performance. The resulting heterostructures were analyzed by optical microscopy, atomic force microscopy (AFM), Raman spectroscopy and high-resolution transmission electron microscopy (HRTEM) . Of particular

View Article Online
DOI: 10.1039/D4NA00935E

significance are the sharp and clean edges and faces of the crystals, indicating high-quality interfaces of the heterostructures.

EXPERIMENTAL SECTION

Materials. $CrCl_3$ (Alfa Aesar, anhydrous 99.9%), MoO_3 (99.9995%, thermo scientific, melting point: 795 ℃), S (metals basis 99.9995%, thermo scientific, boiling point: ~ 445 ℃), KCl (99.999%, Sigma Aldrich).

Thermodynamic simulations using TRAGMIN software. Thermodynamic simulations were performed with a modified version of the software "TRAGMIN 5.1". The used thermodynamic data of all species were taken from the FactPS database [34] and a list of the used species is given in the SI. A system volume of 9.4 mL was used, as well as $5\cdot10^{-9}$ mmol H_2O and $1\cdot10^{-9}$ mmol Ar traces were added for all simulations.

Preparation and pretreatment of substrates. *c*-sapphire (0001) wafers were cut to substrates with specific dimensions ($10.0 \times 5 \times 0.5$ mm^3). Photoresist was spun onto the wafers to protect the polished surface from damage during the cutting process. To remove the photoresist afterwards the substrates were rinsed with acetone and cleaned by ultrasonic treatment in distilled water for 15 min. Afterwards, they were rinsed again with distilled water and excess liquid removed with compressed nitrogen. Finally, the substrates were annealed in air as described in Figure S1.

Synthesis of $CrCl_3/MoS_2$ by sequential CVT.

For the synthesis of MoS_2 nanolayers, the starting materials were mixes in a glovebox with the ratio MoO_3:S = 1:2. One milligram of this mixture was placed in the source side of the ampoule, with approximately 1 milligram of KCl utilized as the transport agent. A *c*-sapphire (0001) substrate was positioned in the sink side of the ampoule and sealed by vacuum sealing line (oxyhydrogen flame) at a pressure of ~ 2×10^{-3} mbar. For the growth process, the two-zone LOBA furnace (HTM Reetz, GmbH) was set to the following temperatures T1 = 1000 ℃; T2 = 800 ℃ for 30 min, followed by natural cooling. The ampoules were opened in the glovebox, and the substrate was transferred to a new ampoule. In the second ampoule approximately 5 milligrams of $CrCl_3$ were put in the source side and to the sink side the substrate is transferred. The growth conditions for the second step was 600 ℃ at the source side and 500 ℃ in the sink side as shown in Figure S2. The ampoule was quenched in water after 15 min.

View Article Online
DOI: 10.1039/D4NA00935E

Preparation of the TEM lamella. To analyze the cross-section of the $CrCl_3/MoS_2$ heterostructure using TEM, a lamella in the overlapped region of the $CrCl_3/MoS_2$ heterostructure was prepared by focused ion beam (FIB) cutting. The preparation was carried out using a Helios 5 CX (Thermo Scientific). Initially, the sample was coated with a 20 nm carbon layer using a sputter coater, followed by electron beam-induced deposition (EBID) and ion beam-induced deposition (IBID) for additional protection and stability. The FIB cutting was performed at an acceleration voltage of 30 kV and a current of 2.5 nA to create the initial trenches, followed by a lower current for the final polishing to ensure minimal damage to the sample. This multi-step coating and cutting process ensured the sample's integrity during FIB milling and subsequent TEM analysis. The precise FIB technique allowed for the accurate extraction of a thin lamella, crucial for detailed cross-sectional TEM studies.

Characterization

Optical Microscopy. After breaking the ampoule, the first characterization of the crystal morphology was conducted using an optical microscope (Keyence VHX-7000) equipped with a VHX-7020 CMOS image sensor.

Scanning Electron Microscopy (SEM) and Energy Dispersive X-ray Spectroscopy (EDX). Morphological and compositional analyses were performed using scanning electron microscopy (SEM) at various magnifications, coupled with energy dispersive X-ray spectroscopy (EDX) using a FEI Nova-NanoSEM 200. The EDAX Genesis Spectrum software was used to measure the composition of the crystals. 5 measurements at different spots/crystals were averaged to calculate the composition of each crystal or experiment.

Raman Spectroscopic Investigations. These measurements were performed using a T64000 Raman Spectrometer (Horiba Jobin Yvon) under 532 nm laser excitation. The spectra were recorded at room temperatures and utilizing 1800 gr/mm grating.

Transmission Electron Microscopy (TEM). As-grown MoS_2 layers were transferred onto TEM grids (Lacey-carbon 200 mesh Cu, Plano GmbH). Briefly, MoS_2 on the *c*-sapphire (0001) substrate was immersed in 500 μL of pure ethanol and subjected to ultrasonic treatment for 10 min. Subsequently, several drops of the resulting solution were pipetted onto the TEM grid and allowed to air dry. Then the transferred crystals were examined under an optical microscope before TEM investigation. For the $CrCl_3/MoS_2$ heterostructure, the lamella was prepared by FIB cutting, and then, measured by TEM. The measurements were performed with a HRTEM "FEI Titan^3 80−300" (ThermoFisher Scientific Company), operated at an acceleration voltage of 300 kV and selected area electron diffraction (SAED) over an area of a few nm.

Atomic Force Microscopy (AFM). Atomic force microscopy analysis was conducted in tapping mode at the ambient conditions using TESPA-V2 tips on a "Dimension ICON" with scan Asyst (Bruker, USA). Data analysis was conducted using the "Nanoscope Analysis" software, version 1.8.

THEORETICAL BASIS

To investigate the thermodynamic stability of two potential compounds in one system that are so different in their chemistry like MoS_2 and $CrCl_3$, thermodynamic equilibrium calculations of the complex chemical systems with inclusion of the vapor phase have been performed. Initial results for the temperature dependent vapor pressures and condensed phase stabilities of an equimolar $CrCl_3/MoS_2$ system are displayed in Figure 1.

The calculation results demonstrate that in principle $CrCl_3$ and MoS_2 are stable next to each other over a wide temperature range that is suitable for the vapor phase growth of the desired heterostructures. However above ca. 625 °C a significant decomposition of $CrCl_3$ to $CrCl_2$ sets in, but has no major influence on the predicted vapor pressures.

View Article Online
DOI: 10.1039/D4NA00935E

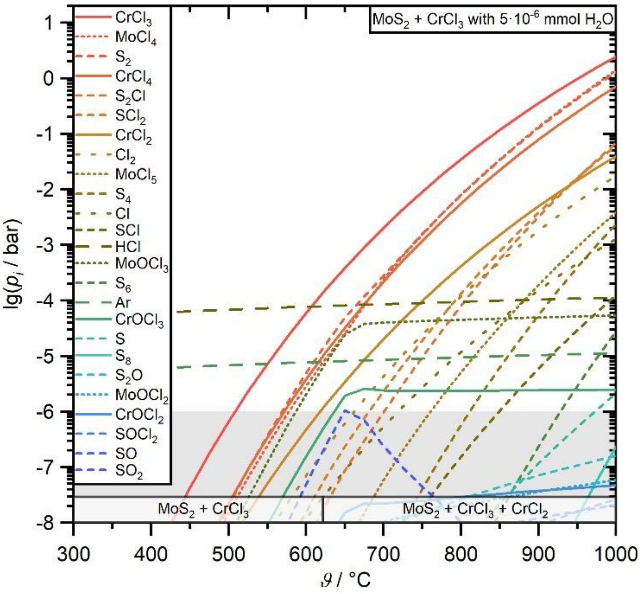

Figure 1. Calculation results of the temperature dependent vapor pressures of the dominating vapor species over an equimolar mixture of MoS_2 and $CrCl_3$ with traces of water. The predicted condensed phases at the bottom are displayed for amounts larger than 10^{-5} mmol. The grey area indicated vapor pressures that are too low for contribution to transport processes.

Based on this initial assessment of thermodynamic stability of the heterostructure, more detailed investigations of potential deposition strategies were performed. While studies for the individual deposition of ultrathin nanosheets of $CrCl_3$ by CVT were already reported [35-37], and can be adapted for the deposition of the first underlying layer of the heterostructure in a sequential deposition strategy, the optimization of the second deposition step on top of the first layer presents an even greater challenge due to the potentially much more complex chemical equilibria in the combined system. To understand this second potential deposition step and to estimate a suitable parameter window for following practical experiments, further calculations of thermodynamic equilibria were combined with CVT models to simulate the transport processes. The primary results for the investigated sequential deposition of $CrCl_3$ on MoS_2 are displayed in Figure 2a. Despite the very small amount of MoS_2 that was used for this simulation to mimic a potentially thin layer of MoS_2 on the substrate, the simulations confirm that a regular deposition of $CrCl_3$ on MoS_2 should be possible at T_{source} above ca. 550 °C that are similar to the individual deposition of $CrCl_3$ nanosheets [35]. The calculated transport efficiencies (Figure 2b) further confirm that the transport process of the $CrCl_3$ is dominated by sublimation and that,

View Article Online
DOI: 10.1039/D4NA00935E

despite the relatively high partial pressures of Mo-containing vapor species (Figure 2a), the transport process is not strongly interfered.

The sequential transport with the opposite order (MoS_2 on $CrCl_3$) with the use of KCl as a transport agent could not be simulated properly, because the use of KCl is most likely generating vapor-phase complexes that are relevant for the transport process but are unknown with respect to both their exact structure and thermodynamic data [38, 39].

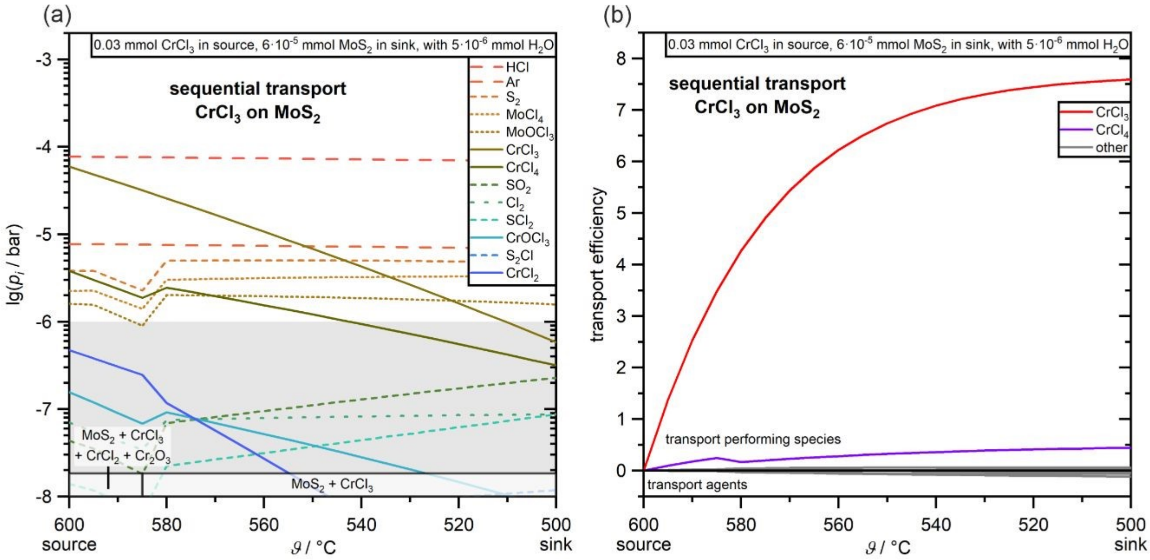

Figure 2. (a) Temperature dependent partial pressures and predicted deposited phases for the simulation of the sequential CVT heterostructure deposition of $CrCl_3$ (starting material in source) on MoS_2 (starting material in sink). For this simulation the source temperature was fixed at 600 °C, while the temperature of the sink was varied between 595 and 500 °C. The grey area indicated vapor pressures that are too low for contribution to transport processes. (b) Calculated transport efficiencies for this simulated CVT.

RESULTS AND DISCUSSION

Growth of MoS_2 as bottom layer of the heterostructure. To optimize the growth of few-layer MoS_2 crystals as a bottom layer via CVT, the precursors molybdenum trioxide (MoO_3), sulfur (S) and potassium chloride (KCl) were used. We varied the synthesis temperatures (500 °C to 1000 °C), the temperature gradient (50 °C – 200 °C) and the transport time (5 min – 60 min). The optimal synthesis parameters include a heating rate of 10 $K.min^{-1}$, with the temperature range maintained between 800 °C and 1000 °C for a duration of 30 min, followed by natural cooling (Figure 3a). This specific heating rate ensures a controlled and uniform temperature

View Article Online
DOI: 10.1039/D4NA00935E

increase, which is crucial for achieving the desired crystalline quality and thickness. Maintaining the synthesis temperature within this range for 30 min allows adequate material deposition and layer formation, promoting the growth of few-layer MoS_2 with minimal defects. The natural cooling process helps in stabilizing the crystal structure, thereby preserving the integrity and uniformity of the MoS_2 layers.

Characterization of the MoS_2. The MoS_2 crystals are uniformly distributed across the substrate in various sizes and exhibit different shapes, including triangular, parallel (where triangular nanosheets stack at 0°), and anti-parallel (where triangular nanosheets stack at 60°). They are stable under ambient conditions. The lateral dimensions of the crystals vary from 10 to 60 µm. Optical images of selected crystals are shown in Figure 3b,c. They exhibit sharp edges and show random twists at different angles: 0° (Figure 3b) and 60° (Figure 3c). The pale blue color resembles a MoS_2 with few layers while the color gradually saturates with increasing number of layers. Notably, under the same temperature gradient conditions, but using a longer transport time (more than one hour), the crystals will become thicker. Additionally, SEM images further support these observations, as shown in Figure S3.

TEM measurements were conducted to confirm the crystallinity and crystal structure. The bright-field TEM image in Figure S5b displays a few tens of nanometer thin MoS_2 flake on the lacey carbon TEM grid. The mono-crystalline layer exhibits an almost hexagonal arrangement in this zone axis orientation (above the highlighted red line in Figure 3d), whereas the superposition of two layers twisted by an in-plane rotation angle of 26° results in a prominent appearance of a so-called Moiré pattern (below the red line in Figure 3d). In fact, the latter is confirmed by image simulations (see Figure S6) using DrProbe software package [40], incorporating the twist angle is determined from the Fourier transform (Figure 3e) of the entire flake from which the HRTEM image in Figure 3d is shown. The diffraction patterns (Figure 3f,g) taken at 001 zone axis orientation exhibit individual reflections that confirm the high crystallinity of the samples. Specifically, the two lines in Figure 3f crossing two reflection pairs, indicating a twisted double layer of MoS_2 with a 13° twisting angle. Similarly, three lines in Figure 3g crossing three reflection pairs, indicating a twisted multi-layer of MoS_2 with twisting angles of 12° and 13°. HRTEM images of a similar flake, also taken at 001 zone axis orientation

View Article Online
DOI: 10.1039/D4NA00935E

(hexagonal space group 194) reveal a twisting between two MoS_2 layers, one extending until the upper edge and one ending 10 nanometer away from the edge. These observations, along with the measured *d*-spacing, confirm that the high crystallinity and precise interlayer alignment of the MoS_2 flakes, validating the twisted bilayer and multilayer structures. More TEM images and their Fourier transforms are provided in Figure S5.

The crystal thicknesses were determined by AFM measurements (Figure 3h-j). Triangular shapes with a thickness of 1.7 nm are observed, corresponding to three layers (Figure 3h). Parallel-oriented triangular nanosheets formed on top of the triangular MoS_2 crystal, are found to exhibit also thicknesses of 1.7 nm, corresponding to three layers, or 2.4 nm, corresponding to four layers (Figure 3i). Anti-parallel oriented nanosheets, are found to have a thickness of 0.8 nm, corresponding to a MoS_2 monolayer (Figure 3j). The AFM images also provide a detailed topographical view of the nanosheets, on the one hand clearly showing the step heights corresponding to the different thicknesses. On the other hand, these high-resolution images highlight the uniformity and smoothness of the nanosheets.

View Article Online
DOI: 10.1039/D4NA00935E

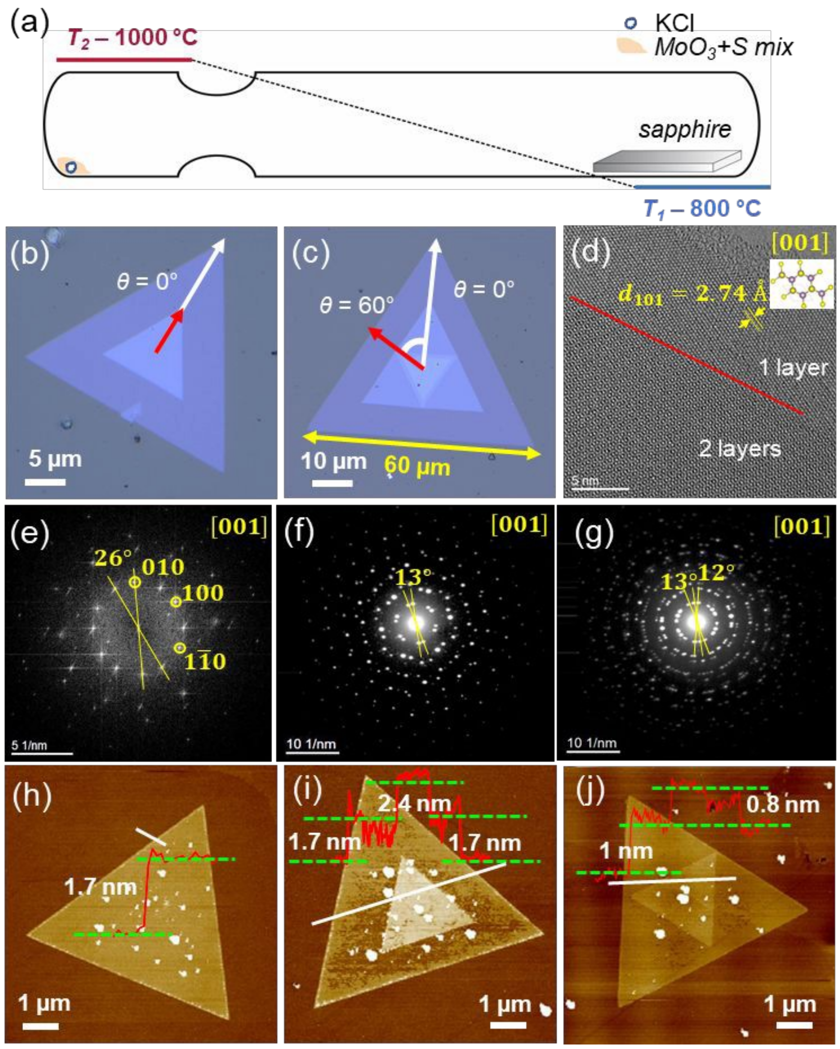

Figure 3. (a) Schematic CVT setup for growth of MoS_2 nanostructures (heating rate 10 K.min^{-1}, T2 = 1000 °C, T1= 800 °C, t = 30 min, naturally cooling). (b,c) Optical microscopy images of twisted MoS_2 stacked in different sizes on *c*-sapphire (0001) substrate. (d) HRTEM image recorded at the edge of a similar MoS_2 flake at 001 zone axis. The inset shows the unit cell in this orientation in which Mo is purple and S yellow. The red line highlights the edge of a second layer twisted by 26° with respect to the first one. (e) Fourier transform of (d) with indexed reflection and indicated twist angle between the two layers. (f,g) Electron diffraction patterns oriented along 001 zone axis (hexagonal space group 194) of the same nanoflake at areas where two (f) and three (g) twisted layers are present. AFM images and height profile measurements of different MoS_2 crystals along the marked white line showing three different shapes: triangular (h), parallel (0°) (i), and anti-parallel (60°) (j).

View Article Online
DOI: 10.1039/D4NA00935E

Growth of $CrCl_3/MoS_2$ Heterostructure. In a second step, $CrCl_3/MoS_2$ heterostructures were prepared and analyzed. The sequential CVT approach involved the deposition of $CrCl_3$ (as a top layer) in a vertical orientation on MoS_2, which had already been grown on a *c*-sapphire (0001) substrate (see Figure 4 and Figure S8). Here, purified $CrCl_3$ (purification process described in Table S1) was used. The growth conditions can be described as follows: T1 = 500 °C; T2 = 600 °C and quenched after 5, 10 or 15 min in tap water using an ampoule catcher [35]. The $CrCl_3$ crystals have a hexagonal shape with very sharp edges and exhibit colors ranging from blue to violet depending on their thickness. The $CrCl_3$ crystals were precisely aligned with the MoS_2 layer so that heterostructures are realized. EDX measurements confirming the composition of $CrCl_3$ are provided in the Figure S7. The thickness of $CrCl_3$ crystals depends on the quenching time. After 5 min of quenching, $CrCl_3$ crystals with a thickness of approximately 15 nm were obtained. If the ampoule is quenched after 2 hours or more, the $CrCl_3$ crystals grew to over 200 nm in thickness. Thus, by varying the CVT conditions, the thickness of the $CrCl_3/MoS_2$ heterostructure can be controlled.

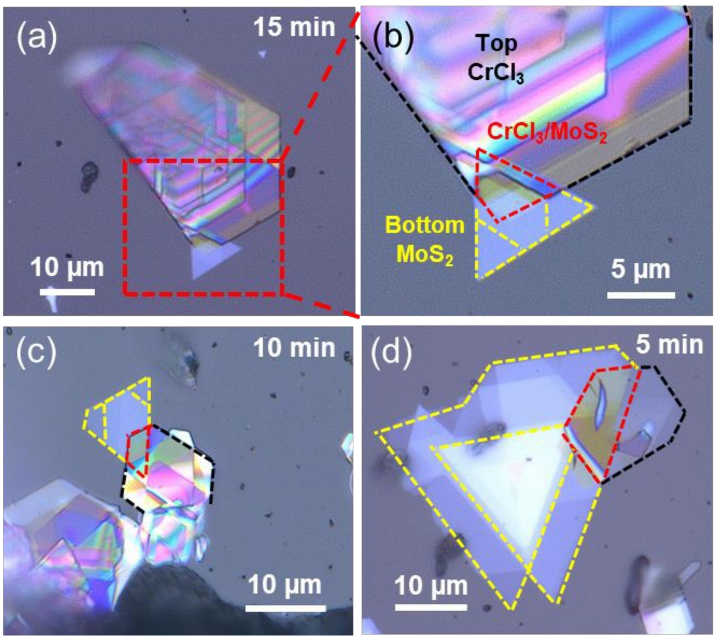

Figure 4. Optical microscope images of $CrCl_3/MoS_2$ heterostructures prepared by sequential CVT. (a) $CrCl_3/MoS_2$ heterostructure with ~ 5 nm $CrCl_3$ layer at overlapped region ($CrCl_3$ was quenched after 15 min). (b) Zoomed-in view of the area marked in (a). (c) $CrCl_3/MoS_2$ heterostructure ($CrCl_3$ was quenched after 10 min). (d) $CrCl_3/MoS_2$ heterostructure after ($CrCl_3$

View Article Online
DOI: 10.1039/D4NA00935E

was quenched after 5 min). Illustrating the uniformity and alignment of the layers stacked atop each other (MoS_2 trigonal shapes with dashed yellow lines and $CrCl_3$ hexagonal shapes with dashed black lines).

Characterization of the $CrCl_3/MoS_2$ heterostructure. AFM images of a selected $CrCl_3/MoS_2$ heterostructure were taken to determine their thickness. The thickness of the MoS_2 layer was determined to be 1.4 nm, corresponding to a bilayer, and the $CrCl_3$ layer thickness was found to be 33 nm, corresponding to a multilayer stack, as shown in Figure 5a. In another sample, shown in Figure 5b, the thicknesses of the MoS_2 and $CrCl_3$ layers were found to be 11 nm and 14 nm, respectively. Clear step edges in the height profile, observed when crossing from the MoS_2 layer to the $CrCl_3$ layer, indicate that $CrCl_3$ typically forms a flat stack on MoS_2.

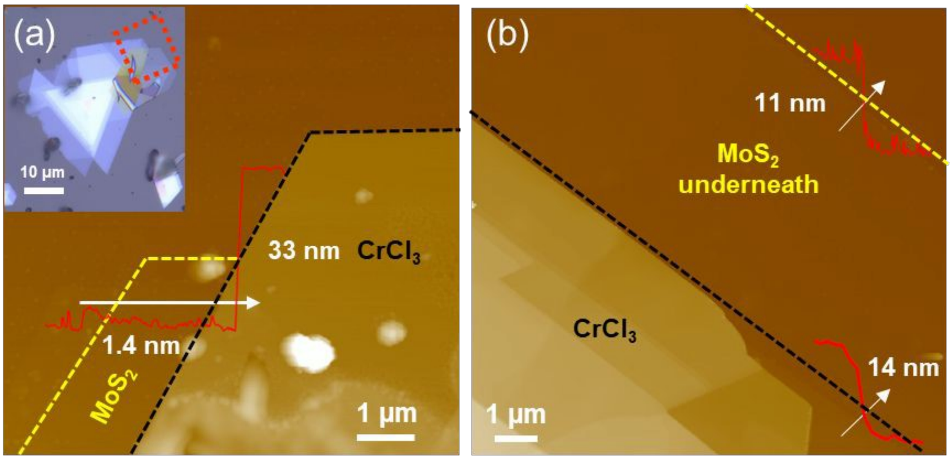

Figure 5. (a) AFM images of $CrCl_3/MoS_2$ heterostructure for the marked region in the optical microscope image (Inset in (a)). (b) AFM image of another $CrCl_3/MoS_2$ heterostructure. Inset: height profile along white arrow shown with the same x-scale as the image scale.

Raman measurements were conducted on the as-grown MoS_2 and $CrCl_3$ layers, as well as the $CrCl_3/MoS_2$ heterostructure, (as illustrated in Figure 6 and Figure S9). The spectra were obtained from different regions, including MoS_2, $CrCl_3$, and the $CrCl_3/MoS_2$ heterostructure. The top blue spectra, representing only MoS_2, exhibit two prominent peaks corresponding to the E^1_{2g} and A_{1g} vibration modes of 2H-MoS_2. These peak positions are consistent with previous reports [41, 42], and corroborate our TEM results obtained. The black spectra at the bottom display six modes that align with the monoclinic phase of the synthesized $CrCl_3$ crystals [16]. The middle

View Article Online
DOI: 10.1039/D4NA00935E

red spectrum, recorded from the $CrCl_3/MoS_2$ heterostructure region, shows all characteristic peaks of both $CrCl_3$ and MoS_2.

Interestingly, no shift in the Raman modes was observed in the heterostructure region compared to the individual layers. Typically, the formation of a heterostructure results in interlayer charge transfer and strain to achieve potential equilibrium and compensate for lattice mismatch at the interface, which often modifies the properties of the individual layers [12, 19]. However, the absence of a shift in the E^1_{2g} and A^1_g modes suggests that the underlying MoS_2 layer remains unaffected by strain and charge doping during the growth process. Similarly, the lack of apparent shift in the Raman modes of $CrCl_3$ indicates a minimal amount of strain in $CrCl_3$ due to lattice mismatch. So, this new synthesis approach can pave the way for innovative advances in growing nanostructures.

This stability in the Raman signal suggests that the semiconductor properties of MoS_2 remain intact even after $CrCl_3$ deposition. The preservation of the characteristic Raman peaks and their intensities indicates that the heterostructure maintains the high crystalline quality and integrity of both the MoS_2 and $CrCl_3$ layers. This result confirms that the sequential CVT technique allows for the successful assembly of $CrCl_3/MoS_2$ heterostructures without affecting the crystallinity of MoS_2.

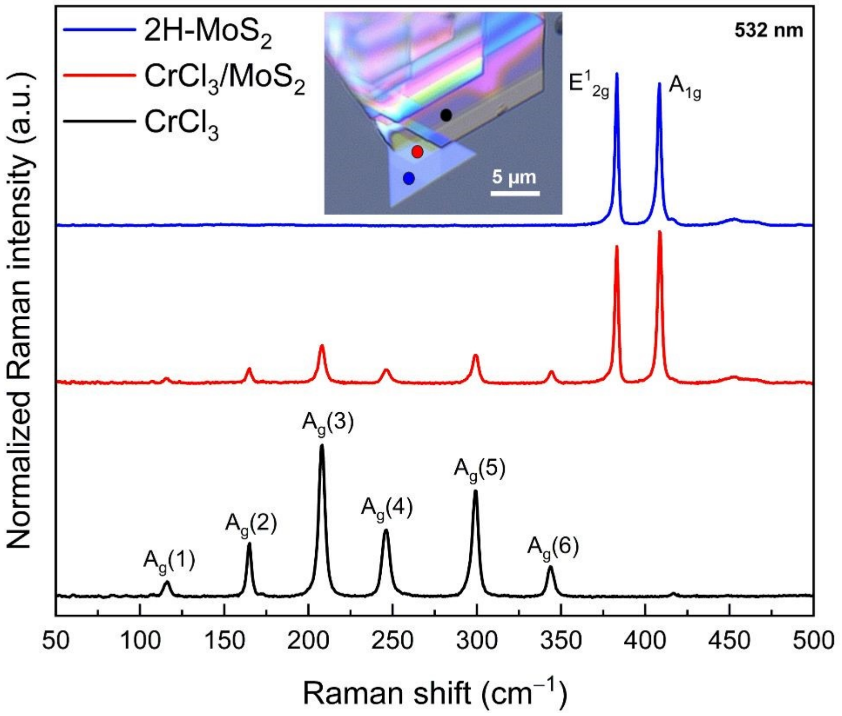

View Article Online
DOI: 10.1039/D4NA00935E

Figure 6. Raman spectra of the $CrCl_3/MoS_2$ vertical heterostructure. Raman spectra taken from the three different regions, labelled in the inset optical microscope image of $CrCl_3/MoS_2$, showing that the anti-parallel triangles of MoS_2, and $CrCl_3$ on the top. There are overlapping Raman signatures with MoS_2 (red line).

The SEM and cross-sectional HRTEM images of the $CrCl_3/MoS_2$ heterostructure (Figure S10 and Figure 7) depict how the different layers are attached to each other and the Al_2O_3 substrate. In Figure 7, the 5 nm thin atomically flat 2H-MoS_2 layer is most clearly visible, which shows no indications of lattice impurities and point defects. The separation between different vdW layers remained intact and the d_{003}-spacing between them is determined to 0.63 nm. While on top, an ~ 3 nm thick layer of $CrCl_3$ is identified, reflecting successful heterostructure formation. The hardness of the insulating Al_2O_3 substrate required to use a higher voltage, i.e., ion energy during FIB cutting. This process unfortunately amorphized the $CrCl_3$ layer whereas the MoS_2 was more stable under this process. Additionally, $CrCl_3$ presents a significant challenge due to its susceptibility to damage when exposed to high-energy electron beams and intense laser excitation [43].

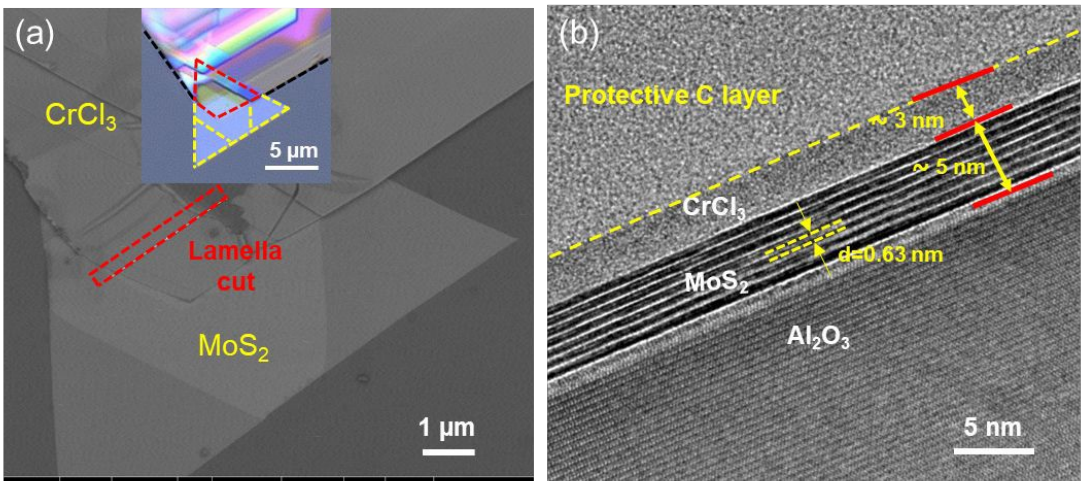

Figure 7. Structural characterization of $CrCl_3/MoS_2$ heterostructure. (a) SEM image of $CrCl_3/MoS_2$ heterostructure, highlighting the marked region for lamella cutting, with the corresponding optical microscope image (Inset in (a)). (b) Cross-sectional HRTEM image of a vertically-staked $CrCl_3/MoS_2$ heterostructure. The image shows the distinct layers of MoS_2 and $CrCl_3$, highlighting their interface and alignment.

View Article Online
DOI: 10.1039/D4NA00935E

CONCLUSIONS

In this study, the synthesis and characterization of $CrCl_3/MoS_2$ vdW heterostructures were comprehensively investigated on *c*-sapphire substrates using a thermodynamically optimized sequential CVT process. The realized structures of MoS_2 exhibit heights down to about 0.8 nm and several μm in lateral size as measured by AFM. Notably, some of these crystals are randomly twisted by different angles in the range of ~ 0° to ~ 60°. The majority of $CrCl_3$ nanosheets exhibit a thickness ranging from 3 to 35 nm, as determined statistically by AFM for several $CrCl_3$ crystals, with large lateral dimensions distributed across the substrate. Notably, thicker crystals are predominantly observed at the substrate edges, with some also present near the center. High-crystallinity and structural quality of both layers were confirmed through Raman spectroscopy and HRTEM. Interestingly, no shift in the Raman modes was observed in the heterostructure which typically will be appear due to strain and interlayer charge transfer to compensate the lattice mismatch at the interface. These kinds of heterostructures creates an optimistic outlook in studying some of interesting physical properties, e.g., magnetic proximity effects in TMDCs. Our method preserves structural integrity, promoting long spin and exciton lifetimes for use in quantum computing and secure communication technologies.

ASSOCIATED CONTENT

SUPPORTING INFORMATION

In the SI section, further details on the CVT synthesis process and workflow are provided, encompassing stepwise procedures, reaction conditions, and optimizations made. Additionally, the purification method for commercial $CrCl_3$ is outlined. Substrate pretreatment techniques, such as cleaning procedures or surface modifications, are also described.

View Article Online
DOI: 10.1039/D4NA00935E

AUTHOR INFORMATION

Corresponding Author

Mahmoud M. Hammo − Leibniz Institute for Solid State and Materials Research Dresden e.V., 01069 Dresden, Germany;

orcid.org/0000-0001-9290-2455

E-mail: m.hammo@ifw-dresden.de

Author contributions

Mahmoud M. Hammo: conceptualization, investigation, data curation, visualization, original draft − writing – review & editing. Samuel Froeschke: simulation,– review & editing. Golam Haider: scientific discussions, and helped in modifying the manuscript in the publication form. Daniel Wolf: TEM measurements and analysis. Alexey Popov: Raman measurements. Bernd Büchner: supervision and proof reading. Michael Mertig: resources, acquisition, supervision and proof reading. Silke Hampel: conceptualization, resources, acquisition, supervision. All authors have given approval to the final version of the manuscript.

Conflicts of interest

The authors declare that there are no competing interests.

Data availability

The data supporting this article have been included as part of the ESI.

Acknowledgments

The authors express their gratitude to Sandra Nestler for substrate cutting, Volker Neu and Dennis Hofmann for assistance with AFM measurements, Sandra Schiemenz, Marco Rosenkranz for conducting Raman, Gesine Kreutzer for aiding with EDX quantification, and Robert Heider and Katrin Wruck for their laboratory support. Almut Pöhl for FIB cutting. Daniel Wolf acknowledges financial support from the Collaborative Research Center

“Chemistry of Synthetic 2D Materials” funded by the Deutsche Forschungsgemeinschaft (DFG, German Research Foundation) – SFB-1415 (417590517). Mahmoud M. Hammo expresses gratitude to the IFW excellence program for its financial assistance. Mahmoud M. Hammo and Michael Mertig acknowledge financial support from the Deutsche Forschungsgemeinschaft (DFG; RTG 2767).

References

1. J. Yao, Z. Zheng and G. Yang, *Advanced Functional Materials*, 2017, **27**, 1701823.
2. H. Zhang, X. Zhang, C. Liu, S.-T. Lee and J. Jie, *ACS nano*, 2016, **10**, 5113-5122.
3. C. Zhong, V. K. Sangwan, C. Wang, H. Bergeron, M. C. Hersam and E. A. Weiss, *The journal of physical chemistry letters*, 2018, **9**, 2484-2491.
4. R. K. Biroju, D. Das, R. Sharma, S. Pal, L. P. Mawlong, K. Bhorkar, P. Giri, A. K. Singh and T. N. Narayanan, *ACS Energy Letters*, 2017, **2**, 1355-1361.
5. S. Bettis Homan, V. K. Sangwan, I. Balla, H. Bergeron, E. A. Weiss and M. C. Hersam, *Nano letters*, 2017, **17**, 164-169.
6. A. K. Geim and I. V. Grigorieva, *Nature*, 2013, **499**, 419-425.
7. B. Tian, Ph.D. Ph.D. Dissertation, King Abdullah University of Science and Technology, 2022.
8. S. K. Behera, M. Bora, S. S. P. Chowdhury and P. Deb, *Physical Chemistry Chemical Physics*, 2019, **21**, 25788-25796.
9. D. Ghazaryan, M. T. Greenaway, Z. Wang, V. H. Guarochico-Moreira, I. J. Vera-Marun, J. Yin, Y. Liao, S. V. Morozov, O. Kristanovski and A. I. Lichtenstein, *Nature Electronics*, 2018, **1**, 344-349.
10. Q. Zhang, S. A. Yang, W. Mi, Y. Cheng and U. Schwingenschlögl, *Advanced Materials*, 2016, **28**, 7043-7047.
11. M.-C. Heißenbüttel, T. Deilmann, P. Krüger and M. Rohlfing, *Nano letters*, 2021, **21**, 5173-5178.
12. L. Ciorciaro, M. Kroner, K. Watanabe, T. Taniguchi and A. Imamoglu, *Physical Review Letters*, 2020, **124**, 197401.
13. A. Rasmita and W.-b. Gao, *Nano Research*, 2021, **14**, 1901-1911.
14. X. Cai, T. Song, N. P. Wilson, G. Clark, M. He, X. Zhang, T. Taniguchi, K. Watanabe, W. Yao and D. Xiao, *Nano letters*, 2019, **19**, 3993-3998.
15. M. A. McGuire, G. Clark, K. Santosh, W. M. Chance, G. E. Jellison Jr, V. R. Cooper, X. Xu and B. C. Sales, *Physical Review Materials*, 2017, **1**, 014001.
16. D. R. Klein, D. MacNeill, Q. Song, D. T. Larson, S. Fang, M. Xu, R. A. Ribeiro, P. C. Canfield, E. Kaxiras and R. Comin, *Nature Physics*, 2019, **15**, 1255-1260.
17. J. Zhao, X. Jin, H. Zeng, C. Yao and G. Yan, *Applied Physics Letters*, 2021, **119**.
18. K. L. Seyler, D. Zhong, B. Huang, X. Linpeng, N. P. Wilson, T. Taniguchi, K. Watanabe, W. Yao, D. Xiao and M. A. McGuire, *Nano letters*, 2018, **18**, 3823-3828.
19. T. P. Lyons, D. Gillard, A. Molina-Sánchez, A. Misra, F. Withers, P. S. Keatley, A. Kozikov, T. Taniguchi, K. Watanabe, K. S. Novoselov, J. Fernández-Rossier and A. I. Tartakovskii, *Nature Communications*, 2020, **11**, 6021.
20. J. Choi, C. Lane, J.-X. Zhu and S. A. Crooker, *Nature Materials*, 2023, **22**, 305-310.
21. Ł. C. Kipczak, Z.; Huang, P.; Vaklinova, K.; Watanabe, K.; Taniguchi, T.; Babiński, A.; Koperski, M.; Molas, M. R., *arXiv preprint arXiv:2304.11896*, 2023, DOI: 10.48550/arXiv.2304.11896.
22. J. F. Sierra, J. Fabian, R. K. Kawakami, S. Roche and S. O. Valenzuela, *Nature Nanotechnology*, 2021, **16**, 856-868.
23. X. Yin, C. S. Tang, Y. Zheng, J. Gao, J. Wu, H. Zhang, M. Chhowalla, W. Chen and A. T. Wee, *Chemical Society Reviews*, 2021, **50**, 10087-10115.

View Article Online
DOI: 10.1039/D4NA00935E

24. P. Rivera, J. R. Schaibley, A. M. Jones, J. S. Ross, S. Wu, G. Aivazian, P. Klement, K. Seyler, G. Clark and N. J. Ghimire, *Nature communications*, 2015, **6**, 6242.
25. D. Zhong, K. L. Seyler, X. Linpeng, N. P. Wilson, T. Taniguchi, K. Watanabe, M. A. McGuire, K.-M. C. Fu, D. Xiao, W. Yao and X. Xu, *Nature Nanotechnology*, 2020, **15**, 187-191.
26. C. Boix-Constant, S. Mañas-Valero, R. Córdoba, J. J. Baldoví, Á. Rubio and E. Coronado, *ACS nano*, 2021, **15**, 11898-11907.
27. Y. Xia, J. Zha, H. Huang, H. Wang, P. Yang, L. Zheng, Z. Zhang, Z. Yang, Y. Chen and H. P. Chan, *ACS Applied Materials & Interfaces*, 2023, DOI: 10.1021/acsami.3c06316.
28. J. McKenzie, N. Sharma and X. Liu, *APL Materials*, 2024, **12**.
29. A. V. Kretinin, Y. Cao, J.-S. Tu, G. Yu, R. Jalil, K. S. Novoselov, S. J. Haigh, A. Gholinia, A. Mishchenko and M. Lozada, *Nano letters*, 2014, **14**, 3270-3276.
30. F. Liu, *Progress in Surface Science*, 2021, **96**, 100626.
31. Y. Gong, J. Lin, X. Wang, G. Shi, S. Lei, Z. Lin, X. Zou, G. Ye, R. Vajtai and B. I. Yakobson, *Nature materials*, 2014, **13**, 1135-1142.
32. S. Hao, X. Ji, F. Liu, S. Zhong, K. Y. Pang, K. G. Lim, T. C. Chong and R. Zhao, *ACS Applied Nano Materials*, 2021, **4**, 1766-1775.
33. R. Ai, X. Guan, J. Li, K. Yao, P. Chen, Z. Zhang, X. Duan and X. Duan, *ACS nano*, 2017, **11**, 3413-3419.
34. C. W. Bale, E. Bélisle, P. Chartrand, S. A. Decterov, G. Eriksson, A. E. Gheribi, K. Hack, I. H. Jung, Y. B. Kang, J. Melançon, A. D. Pelton, S. Petersen, C. Robelin, J. Sangster, P. Spencer and M. A. Van Ende, *Calphad*, 2016, **54**, 35-53.
35. M. Grönke, B. Buschbeck, P. Schmidt, M. Valldor, S. Oswald, Q. Hao, A. Lubk, D. Wolf, U. Steiner and B. Büchner, *Advanced Materials Interfaces*, 2019, **6**, 1901410.
36. S. Froeschke, D. Wolf, M. Hantusch, L. Giebeler, M. Wels, N. Gräßler, B. Büchner, P. Schmidt and S. Hampel, *Nanoscale*, 2022, **14**, 10483-10492.
37. S. Froeschke, N. Yasmen, A. A. Popov, S. Schiemenz, D. Wolf, L. Giebeler, M. Hantusch, N. Gräßler, B. Büchner and P. Schmidt, *Chemistry of Materials*, 2023, **35**, 4136-4148.
38. H. Schäfer, *Angewandte Chemie International Edition in English*, 1976, **15**, 713-727.
39. S. Lopatin and S. Shugurov, *Russian Journal of General Chemistry*, 2019, **89**, 1059-1068.
40. J. Barthel, *Ultramicroscopy*, 2018, **193**, 1-11.
41. H. Cun, M. Macha, H. Kim, K. Liu, Y. Zhao, T. LaGrange, A. Kis and A. Radenovic, *Nano Research*, 2019, **12**, 2646-2652.
42. C. Lee, H. Yan, L. E. Brus, T. F. Heinz, J. Hone and S. Ryu, *ACS nano*, 2010, **4**, 2695-2700.
43. J. Wang, Z. Ahmadi, D. Lujan, J. Choe, T. Taniguchi, K. Watanabe, X. Li, J. E. Shield and X. Hong, *Advanced Science*, 2023, **10**, 2203548.

View Article Online
DOI: 10.1039/D4NA00935E

Data availability

The data supporting this article have been included as part of the ESI.